Fabrication of micro-structured surfaces by additive manufacturing, with simulation of dynamic contact angle

Davoudinejad, Ali; Cai, Yukui; Pedersen, David Bue; Luo, Xichun; Tosello, Guido

Published in:
Materials & Design

Link to article, DOI:
10.1016/j.matdes.2019.107839

Publication date:
2019

Document Version
Publisher's PDF, also known as Version of record

Materials and Design 176 (2019) 107839

Contents lists available at ScienceDirect

Materials and Design

journal homepage: www.elsevier.com/locate/matdes

Fabrication of micro-structured surfaces by additive manufacturing, with simulation of dynamic contact angle

Ali Davoudinejad [a,*], Yukui Cai [b], David Bue Pedersen [a], Xichun Luo [b], Guido Tosello [a]

[a] Department of Mechanical Engineering, Technical University of Denmark, Building 427 A, Produktionstorvet, 2800 Kgs. Lyngby, Denmark
[b] Centre for Precision Manufacturing, DMEM, University of Strathclyde, UK

HIGHLIGHTS

- Direct fabrication of the components with micro structured surfaces by digital light processing method.
- Digital Light Processing method was pushed to its limit for fabrication of the components with micro holes.
- Measurement of the components with micro holes present uniformity of the print in different areas of the structure.
- The printed substrate realized hydrophobicity on the hydrophilic materials (intrinsic contact angle of 65°).
- 3D dynamic impact behavior simulation for contact angle prediction was used to estimate wettability of the surface.

GRAPHICAL ABSTRACT

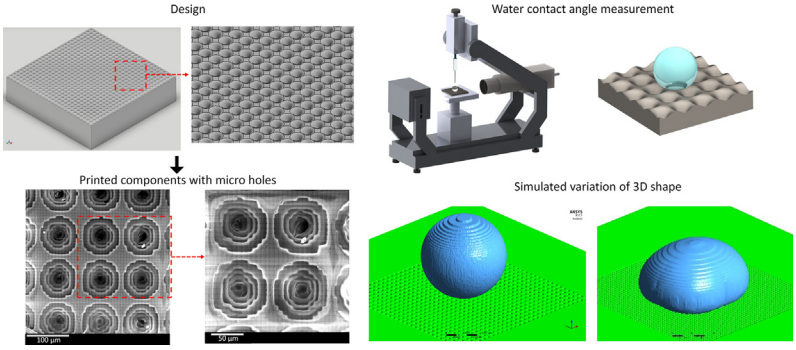

ARTICLE INFO

Article history:
Received 1 March 2019
Received in revised form 6 May 2019
Accepted 7 May 2019
Available online 10 May 2019

Keywords:
Additive manufacturing
Microstructure surfaces
Precision manufacturing
Functional surfaces
Volume of fluid

ABSTRACT

This work presents an Additive Manufacturing (AM) based method for production of components with micro-structured surfaces. Vat photopolymerization was used for the experiments by an AM custom-build machine at the Technical University of Denmark (DTU). Components with micro holes were printed in different sizes and the uniformity of them analyzed. Subsequently, in order to assess the functionality of the surface, the water droplet contact angle was measured to evaluate the wettability of the different components with micro holes. It was found that it was possible to fabricate the components with micro holes using precision AM process. The printed substrate exhibited hydrophobicity as a hydrophilic material (intrinsic contact angle of 65°). A hydrophobic surface was achieved with the printed features exhibiting a maximum contact angle of 113°. Additionally, the volume of fluid (VOF) method was employed to predict the surface contact angle. The predicted results were validated by comparison against the experiments. The average value from experiments was predicted by the model. However, it was noted that the cross-sectional height profile of the structures and the surface roughness of the printed samples, were not precisely replicated as designed, which slightly affects the prediction results, though, similar prediction trend was observed.

1. Introduction

Manufacturing of the components with micro/nano-structured surfaces have been studied for more than a decade with various fabrication methods. Significance and application of such surfaces have been

* Corresponding author.
E-mail address: alidav@mek.dtu.dk (A. Davoudinejad).

https://doi.org/10.1016/j.matdes.2019.107839

enhancing due to great functionality such as withstanding against severe abrasion [1], corrosion resistance [2], chemical industry separation [3], self-cleaning [4], antibacterial surfaces [5], and dynamic fluids transportation [6]. Furthermore, hierarchical surfaces are also used in wall-climbing robots and grippers for other applications [7–9]. The fabrication of these types of features and the functionality of different designs are still challenging for industrial applications because of high production cost and low production efficiency in the prototyping phase. The fabrication technology of these surfaces have been advanced and evolved from traditional manufacturing to more advanced methods in industries.

Additive manufacturing process has undergone outstanding advancement recently and becomes more widespread in different industries for parts production. Particularly due to some advantages compared to traditional manufacturing techniques such as the possibility of fabricating complex geometries, the rational use of materials, the relatively low time consumption and the inherent user friendliness [10]. The vat photopolymerization method is currently used moderately in range of commercial and industrial sectors and can efficiently manufacture complex objects with low cost in a relatively short time [11].

Several manufacturing approaches for fabrication and preparation of microstructured surfaces were investigated. The functional surfaces are frequently fabricated by nanotechnology to create technologically advanced products. However, manufacturing surfaces with microstructure features are generally time-consuming and not economical for mass production [12]. The conventional methods to manufacture microstructure features are for example photolithography, soft lithography, or combination of these two methods, as well as roll-to-roll UV embossing [13,14] and hot embossing [15]. Alternative process chains recently investigated include: dip-transfer to manufacture a 3D printed mold applied to produce water-repellency surfaces [16]; 3D direct laser writing used in two-photon polymerization to structure polymer materials [17]; additive manufacturing (AM) method such as vat photopolymerization used for fabrication of polymer micro features [18,19]. AM was also applied for fabrication of micro scale biomaterials with superior properties [20] and using powder-based additive manufacturing for processing metallic materials [21,22]. Negative additive manufacturing was also applied for sacrificial molds used for casting negative copies for complex shapes [23]. Other methods such as subtractive laser machining process by a nanosecond pulsed fiber laser [24] and micro milling which have been used for several decades due their flexibility and productivity of the method for manufacturing of 3D micro components for diverse materials were applied [25].

Various testing methods were employed on different AM structures in order to investigate the functionality of the surface such as experimental compression tests [26,27], microstructure and dynamic mechanical behavior [28], drop-weight impact testing and rebound dynamics of a drop at various liquid viscosities [29,30]. Moreover, component wettability is a factor to consider in the features fabricated by AM processes [31]. Alongside with the experimental studies, various approaches were applied to simulate flow and dynamic behavior [32,33]. The wetting behavior of the water droplet impact on the structured surfaces is critical to understand the underlying mechanism of hydrophobicity and predict its contact angle. However, it is difficult to clearly observe the details of solid-liquid contact area through experiments due to unfavorable optical measurement condition and short impacting time [34]. For instance, it is very challenging to measure the velocity and pressure of water drops in the impacting process on structured substrate.

In the last decade, many researchers investigated the dynamic behavior of the water droplet impacted on the structured surface, which is intrinsic to the practical applications of superhydrophobic surfaces. Molecular dynamics simulation (MDS), lattice Boltzmann method (LBM) and volume of fluid (VOF) method are three primary numerical methods for studying superhydrophobic problems. J. Yan et al. [14] investigated the impact phenomenon of a nano-sized water droplet on a pillared graphite surface by MDS conducted for 1 ns with a time interval of 2 fs. The results showed that the decrease of the gaps leads to a higher contact angle and the increase of the height of pillars increase the critical velocity of the wetting transition. Sandip Khan [35] et al. also used MDS to study the transition between Wenzel state and Cassie state with varying the pillar height. The numerical analysis showed that it would take 500–600 ps to reach the equilibrium state. W. Xu [36] et al. explored heterogeneous nucleation of water droplet on surfaces with different surface free energies. The time step of 2 fs was chosen in their research, and each simulation was only carried out for 2 ns. Thus, MDS is effective at nano-scale and ns level, but not suitable to study large length and time scale, for example in millimeter and ms level due to low efficiency. LBM is a mesoscale modelling method, which is also developed to model the superhydrophobic phenomenon. Kevin [37] et al. calculated forced wetting under the gravity of a drop on the pillared superhydrophobic surface by LBM. The authors reproduced boundary conditions of the experimental contact angles of drops on a superhydrophobic surface. Lizhi [38] et al. also utilized LBM to investigate the dynamic behavior of coalesced droplet jumping on the superhydrophobic surface with randomly distributed rough structures. The timescale used in their simulation varied from microsecond to 20 ms. However, the observation results by high-speed camera approved that the impacting process of water droplet does not reach a stable state after 20 ms [39].

VOF method is a fixed-mesh method, in which the interface between immiscible fluids is modelled as the discontinuity in characteristic function (such as volume fraction) [40]. Thus, VOF simulation can analyze

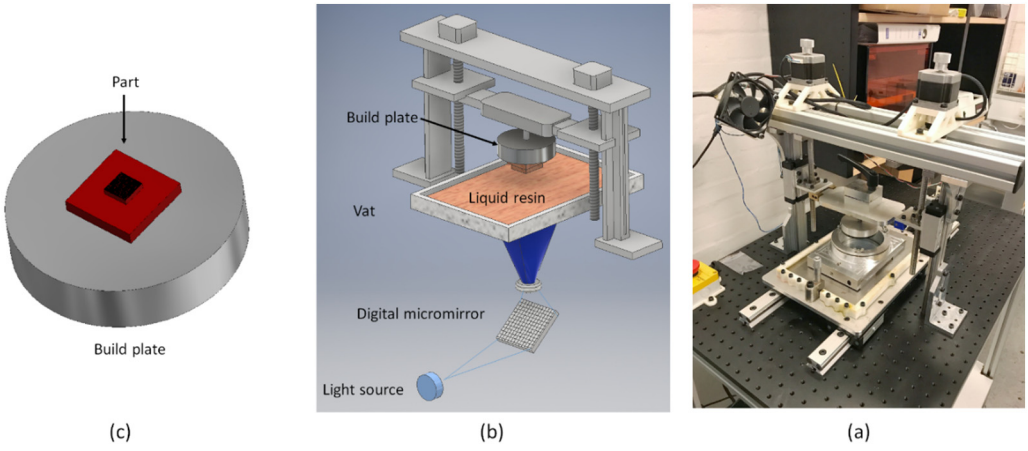

Fig. 1. (a) Experimental set-up DLP 3D printer (b) The schematic of the DLP technology bottom-up projection 3D printing process. (c) Printed part direction on build plate.

Table 1
Experimental conditions [49].

Parameters	Selected parameters
Layer thickness/μm	15
Exposure time/s	3.5
Photopolymer resin	FTD red pigment
Printing resign temperature/°C	23

the wetting state of different cases thus saves the time of fabricating and testing of different substrates. In recent years, VOF simulations of droplet impacted on structured surface have also been reported by some researchers [41–43]. Prashant [42] et al. simulated drop impacting on smooth surface with lower impact velocities. Jinliang [43] et al. investigated drop impacting on heterogeneous surface by VOF. The authors explored the relationship between non-dimensional parameters (Weber number and Ohnesorge number) and state of droplet. Karthik [44] et al. performed 3D VOF simulation and concluded that it has similar behavior as the 2D case for the same initial conditions. They also described that the entry of the drop into the gap between the pillars depends on the water hammer pressure.

The above studies investigated the dynamic behavior of the water droplet. However, limited studies reported on the prediction of the apparent contact angle of the structured surface in an equilibrium state, which can be employed to confirm the design parameters with best hydrophobicity before production. In this study, vat photopolymerization, which is a well-known (AM) process, used for fabrication of the components with micro holes. The experimental fabrication capability was investigated and the functionality of the features was tested by wettability assessment of the surfaces. 3D VOF was employed to simulate water droplet contact angle on various structured surfaces and the results were compared against the experiments.

2. Methodology

2.1. Additive manufacturing

The vat photopolymerization method was used as AM process [45]. The process principle is based on liquid photopolymer material in a vat, which is selectively cured by light activated polymerization. This method uses a Digital Light Processing (DLP) projector with optical micro-electro-mechanical technology that uses a Digital Micromirror Device (DMD) to selectively cure the photopolymer material. The light is projected from a source into the DMD and out of the optical lens of the projector. The workpiece in this method is produced on the build platform suspended upside down inside the polymer resin. [46]. The CAD model is used for creation of the parts and sliced for fabrication, each slice with specific pattern is projected onto the bottom layer of the resin tank. The primary layer of the light-sensitive resin cured in a selected exposure time, afterward the next layer is shaped over the previous one to make the feature [47].

The AM machine for experimental photopolymerization used for this study was engineered, built and validated at the AM Laboratory of the Technical University of Denmark [48,49]. Fig. 1(a) shows the AM machine and Fig. 1(b) shows the schematic of the DLP principle bottom-up projection-based. The fabrication of the part started on the build plate and the features were oriented along with the *Z* direction perpendicular to build plate. The build-stage resolution in the vertical direction is 0.4 μm, and the projection mask pixel spacing is 7.6 μm in the image plane. The light source of the machine tool is based on a LUXBEAM RS WQ *WQXGA* projector and equipped with a Projection Lens LRS-10 P/N 6501980 with x1 magnification [50]. This projector has a DMD with a 2560 × 1600 pixels array and an image plane size of 20.736 × 11.664 mm (corresponding to a 7.6 μm pitch as already mentioned above). The vertical stage of the machine tool is based upon GTen spindles with zero backlash couplings and an error of ±8 μm. The machine employs ISEL LFS-12-10 precision steel shaft guide rails with pillow blocks and the vertical stage assembly is resolved into 0.4 μm increments at the encoded positioning accuracy limit. The printing process is carried out in different steps from CAD model, selecting the printing parameters (layer thickness, exposure time, etc.), slicing and printing the part. According to prior investigation [49], carried out for characterization of hierarchical microstructure surfaces produced by AM processes by using the same AM method, using design of experiment (DOE). The effects of the layer thickness and exposure time on the final quality were evaluated. Subsequently, the selected process parameters for this experiment are shown in Table 1. The print direction for all samples was perpendicular to the build plate as shown in Fig. 1(c).

Following AM, the next step is the post-processing, which has high impact on the final part shape. Cleaning should be applied to the part that is covered with uncured polymer resin. A bath of isopropanol in a vibration plate ultrasonic cleaner bath (Fig. 2(a)) was used to remove uncured resin. The samples were cleaned in different positions in order to find out the best position for removing the excess resin from the components with microstructures. The efficient method as shown in Fig. 2(c) was clamping the sample upside down in the top of bath in the isopropanol. Next, pressurized air was used for drying the samples. Lastly, post-curing was applied to make sure no reactive resin

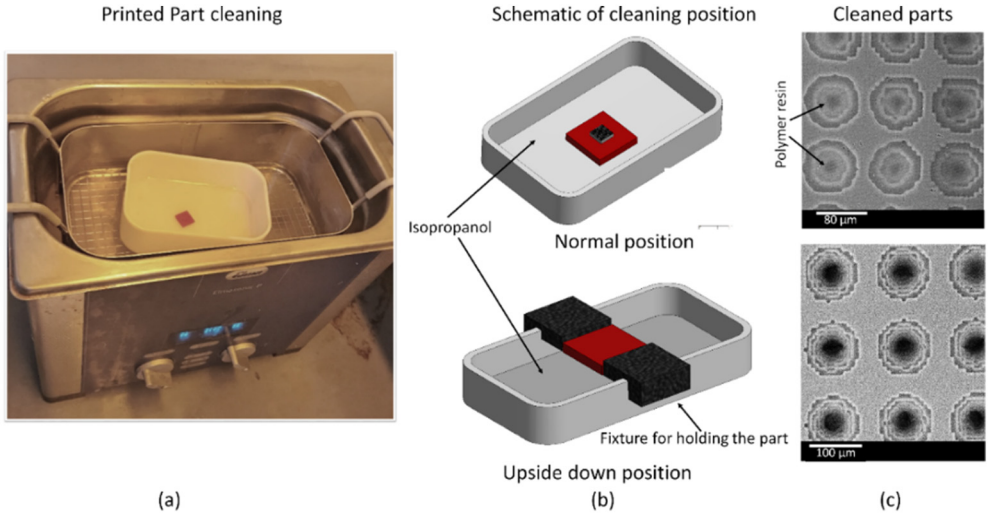

Fig. 2. Post-processing, cleaning the printed samples (a) ultrasonic cleaner bath (b) cleaning positions (c) SEM image of the samples cleaned in different positions.

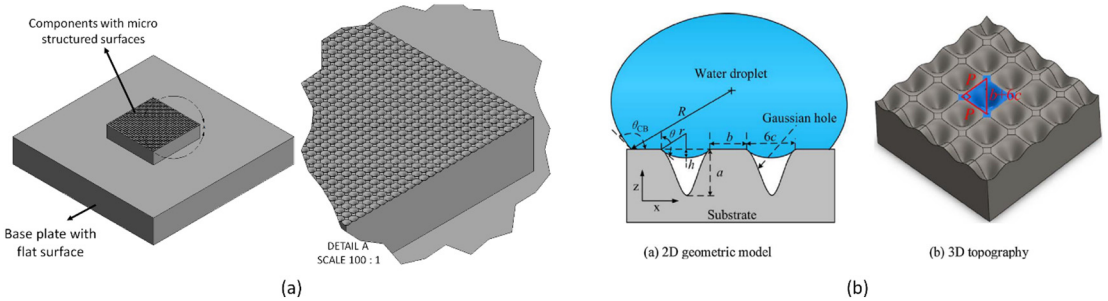

Fig. 3. Features design (a) micro-holes arrays 150 μm pitch (b) 2D Geometric model and 3D topography.

residue is left on the samples and ideal mechanical properties are reached. The printed and post-processed components were exposed in a UV chamber with a diffuse UV light with an irradiant flux density of 300 W/m^2 for 30 min.

3. Surface design

A hole with Gaussian shaped wall profile can be characterized by the Gaussian function as shown in Eq. (1). Thus, the curve between ±3c was chosen to generate the 3D Gaussian hole by CAD software as shown in Fig. 3(b).

$$y = -a \times e^{-\frac{x^2}{2c^2}} \tag{1}$$

The Gaussian-hole models were designed with different pitches and depths in the micro dimensional range as shown in Table 2. All cases have structures with different pitches according to the previously optimized design parameters [14].

Components with micro holes arrays designed for this experiment is shown in Fig. 3(a). P is the pitch between two adjacent holes (Fig. 3(b)). The pitch (P) differs from 50, 70, 110 and 150 μm for samples. However, for each sample, the pitches are the same in the vertical and horizontal directions. The samples consist of a rather thick base for easier handling and removing the samples from build plate.

Table 2
Designed dimensions of Gaussian hole model.

Case run	Test	Surface pattern	P (μm)	*a* (μm)	6c (μm)
1	P50	Gaussian hole arrays	50.0	51.7	57.0
2	P70	Gaussian hole arrays	70.0	69.0	78.6
3	P110	Gaussian hole arrays	110.0	86.0	114.6
4	P150	Gaussian hole arrays	150.0	110.9	153.6

4. Measurement

4.1. Geometrical measurements

In order to evaluate the printed components with micro holes with 150 μm and 110 μm pitch features were selected for analyzing the result of the experiments as shown in Fig. 4. Measurements were carried out on an Alicona Infinite Focus 3D microscope. The measurement procedure consisted in a stratified sampling, where each structured surface was divided into five regions (Fig. 4(a)), where each region was subjected to a randomized sampling. Using this approach, the dimensional representativeness is improved while reducing measurement errors. In addition, a scanning electron microscope (SEM) was used for observation of the samples. Due to the non-conductivity of the polymeric material, a layer of carbon (5–10 nm thickness) was deposited onto the samples prior to SEM imaging.

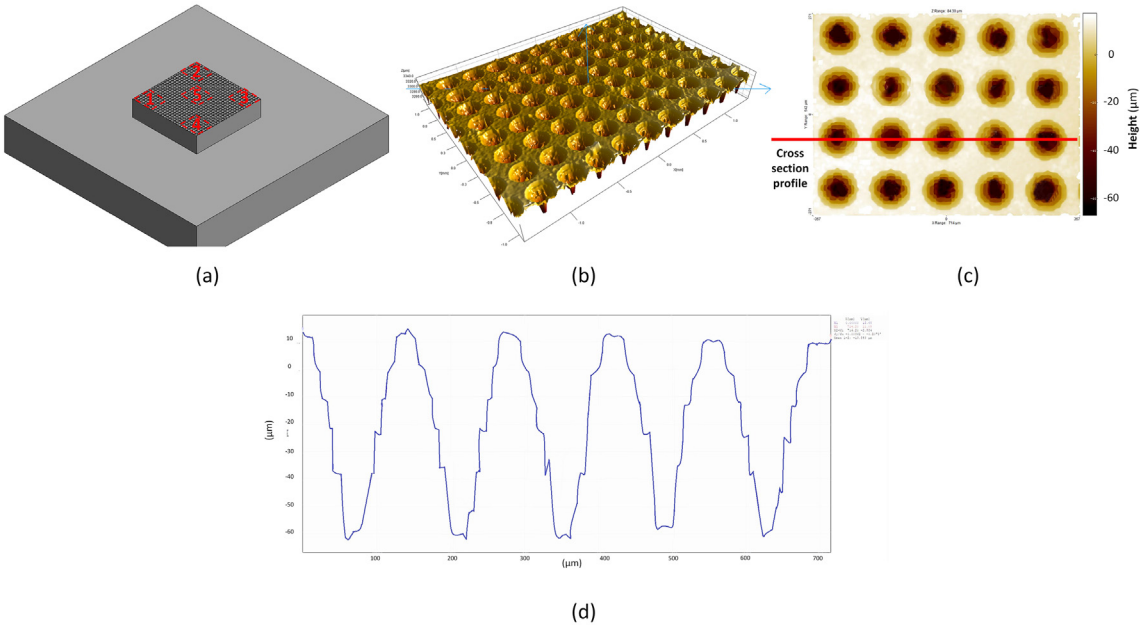

Fig. 4. Acquisition of the measured components with micro holes (a) top view and different measurement positions (b) 3D view of the acquisition (c) height measurement 20× magnification (d) cross section of height profile.

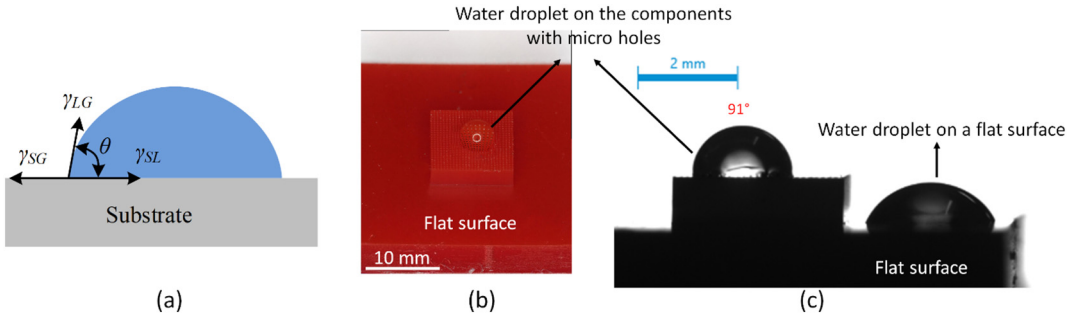

Fig. 5. (a) Schematic of contact angle (b) printed sample (c) water drop on the components with micro holes and flat surface (side view).

4.2. Definition of water contact angle and its measurements

As shown in Fig. 5(a), the contact angle θ is defined as the angle formed by a liquid at the three-phase boundary where a liquid, gas, and solid intersect [51]. For a smooth surface, the contact angle can be expressed by Young's equation using surface tensions between among solid, liquid and gas. Young's equation is expressed as [52].

$$\cos\theta = \frac{\gamma_{SG} - \gamma_{SL}}{\gamma_{LG}} \tag{2}$$

where γ_{LG}, γ_{SG}, γ_{SL} are the interfacial tensions coefficient at liquid/gas, solid/gas, and liquid/solid interfaces, respectively. For a determined material, its intrinsic contact angle can be calculated using Young's equation and measured by the contact angle on a smooth surface. The measurement results of intrinsic contact angle are the basic condition in the simulation setup [52].

In order to characterize hydrophobicity of various structure substrates, the contact angles of water droplets were measured using the sessile drop method by a drop shape analyser (Kruss Ltd.). The selected water droplet volume was 5 μL. For each sample, the contact angle of the water droplet was measured three times and the average value was adopted. Fig. 5(b) shows the printed components with micro holes and Fig. 5(c) illustrates micro holes 150 μm pitch with measured water drop of 91° ± 2.2. For benchmarking, the water drop on a smooth flat surface of the same material was also measured, on the step next to it as 65° ± 3.8, which can be regard as the intrinsic contact angle of photopolymer material (Fig. 5(c)).

5. 3D model for contact angle prediction based on characteristics of micro Gaussian hole

5.1. Mathematical model of VOF method

The VOF method can be applied on two or more immiscible fluids by solving a series of momentum equations and tracking the volume fraction of every fluids throughout the domain [53]. In this study water droplet impacting process is considered to take place at room temperature and the process is adiabatic. Ansys-CFD solver was employed for simulation. The general form of the mass conservation equation is shown in Eq. (3), which is valid for both incompressible and compressible flows.

$$\frac{\partial \rho}{\partial t} + \nabla\cdot\left(\rho\vec{v}\right) = S_m \tag{3}$$

where ρ is density, t is time, and $\vec{v}$ is fluid velocity. S_m represents the source item, which means the mass added to the continuous phase from another phase or other phase. S_m is zero in this research. G. K. Batchelor et al. described the conservation of momentum as [54]:

$$\frac{\partial}{\partial t}\left(\rho\vec{v}\right) + \nabla\cdot\left(\rho\vec{v}\,\vec{v}\right) = -\nabla p + \nabla\cdot(\tau) + \rho\vec{g} + \vec{F} \tag{4}$$

where p is the static pressure, τ is the stress tensor and expressed in Eq. (5). $\vec{g}$ is the acceleration of gravity, $\vec{F}$ is the external body forces.

$$\tau = \mu\left[\left(\nabla\vec{v} + \nabla\vec{v}^{T}\right) - \frac{2}{3}\nabla\cdot\vec{v}I\right] \tag{5}$$

where μ is the molecular viscosity, I is the unit tensor, and the second term on the right side is the effect of volume dilation.

For a single water droplet, the surface tension has a significant effect on its impacting behaviour. The continuum surface force (CSF) model developed by Brackbill [55] et al. was used in this research to consider the surface tension effect. In the CSF model, the volume force ($\boldsymbol{F_{vol}}$) of surface tension to the VOF numerical is a source term $\vec{F}$ in the Eq. (4). For two-phase numerical calculation, the phases are represented by the subscripts 1 and 2. The volume force ($\vec{\boldsymbol{F}}_{\boldsymbol{vol}}$) can be expressed by Eq. (6), k_1 is the curvature of first phase and can be expressed by Eq. (7), $\hat{\boldsymbol{n}}_{\boldsymbol{1}}$ is the unit normal as described in Eq. (8).

$$F_{vol} = \sigma_{12}\frac{\rho k_1 \nabla\alpha_1}{\frac{1}{2}(\rho_1 + \rho_2)} \tag{6}$$

$$k_1 = \nabla\cdot\hat{n}_1 \tag{7}$$

$$\hat{n}_1 = \frac{\nabla\alpha_1}{|\nabla\alpha_1|} \tag{8}$$

where, σ_{12} is the surface tension coefficient between two phases, and α_1 is the volume fraction of first phase.

The intrinsic contact angle (θ) provides information about the wettability of ideal smooth surface. Normally, it comes from the test results. In the VOF simulation, θ is not imposed on the wall itself, but it is used to adjust the surface normal in cells near the wall [55]. Hence, it results in the adjustment of the curvature of the surface near the wall. The surface unit normal at the live cell next to the wall is represented as Eq. (8).

$$\hat{n} = \hat{n}_{wall}\cos\theta + \hat{t}_{wall}\sin\theta \tag{9}$$

Table 3
Computational setup in VOF simulation.

Parameter	Setting/value
Primary phase	Air
Second phase	Water
Calculation type	Transient model
Calculation model	Volume of fluid
Diameter of water droplet (D0)	2.12 mm (5 μL)
Surface tension	0.073 N/m
Intrinsic contact angle	65°
Time step	$1.0 * 10^{-5}$ s

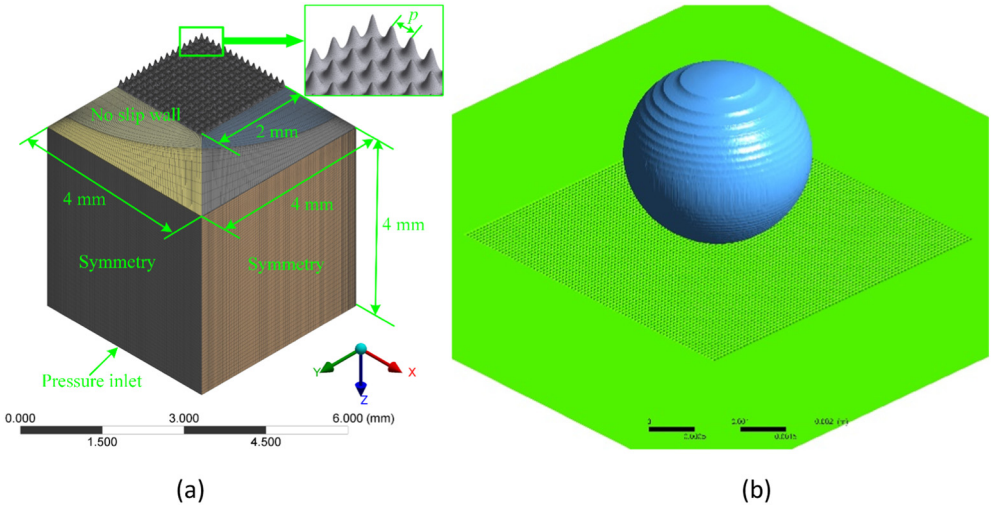

Fig. 6. (a) 3D geometry model of fluid domain based on Gaussian characters (b) Initial state of water droplet for the array with pitch = 50 μm.

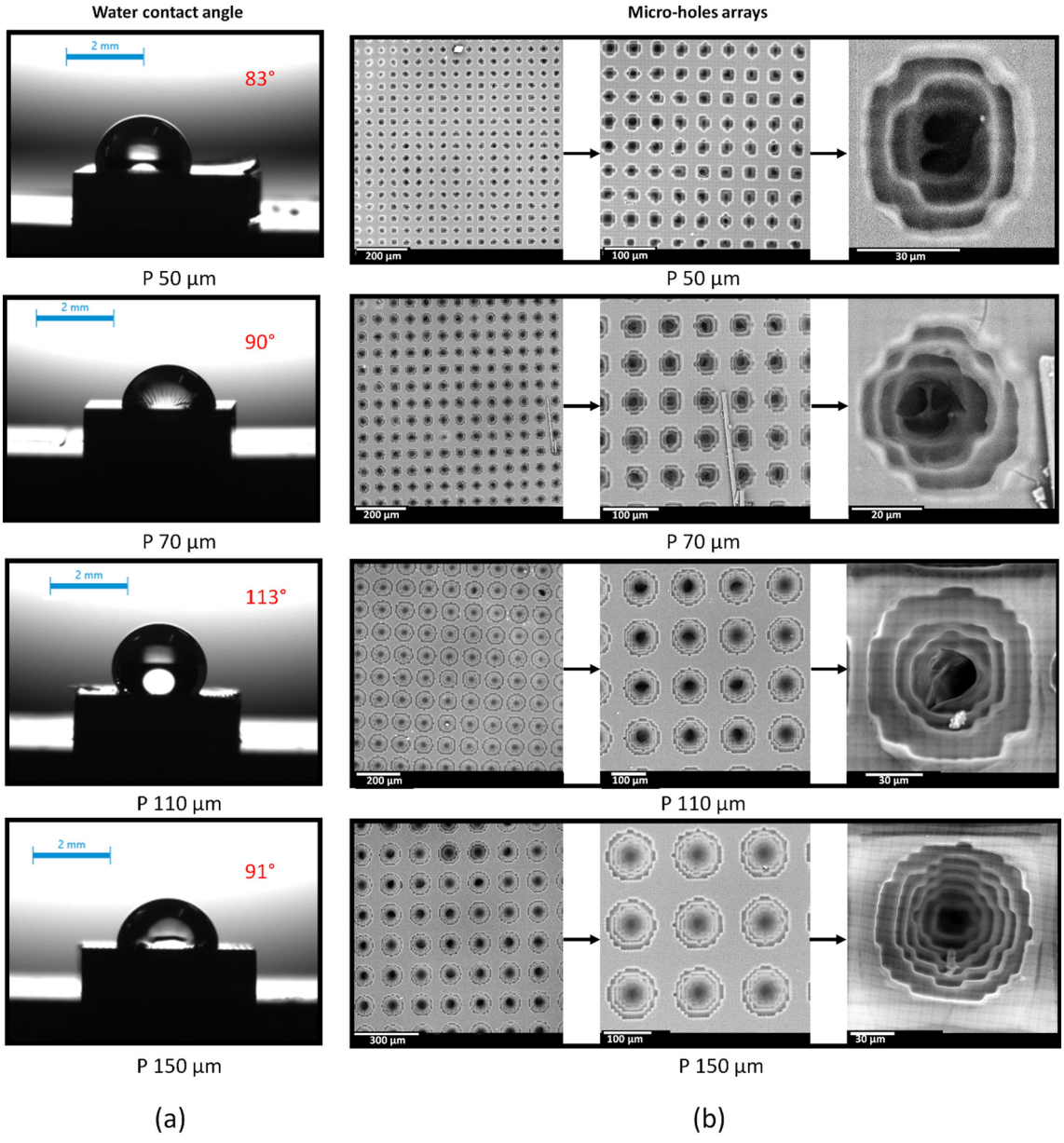

Fig. 7. (a) Water contact angle on microstructures of different pitches (b) SEM pictures of the samples in different sizes and magnifications.

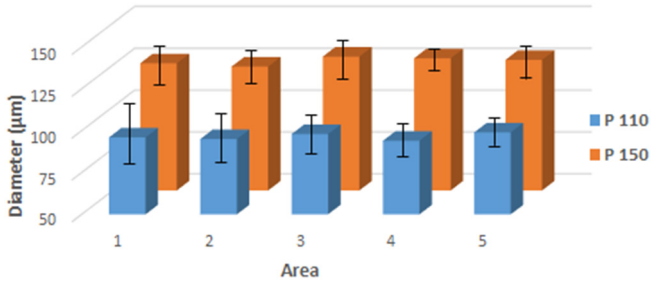

Fig. 8. Diameter of printed features in different areas.

where $\hat{n}_{wall}$ and $\hat{t}_{wall}$ are the unit vectors normal and tangential to the wall, respectively. The Weber number (We), is often useful in analyzing fluid flows of an interface between two different fluids, is a dimensionless parameter. It represents the ratio of the inertial force to the surface tension force. The Weber number (We) is given by Eq. (10).

$$\mathrm{We} = \frac{\rho v^2 l}{\sigma} \tag{10}$$

where l is its characteristic length, typically the droplet diameter.

5.2. Computational setup

The 3D geometry models used in the VOF simulation are based on Table 2. The water droplet spreading behaviour of four different structures surface with pitch from 50 to 150 µm were simulated by VOF method. The computational setup for the VOF simulation is shown in Table 3.

Since the model with Gaussian shaped hole and water droplet are symmetric, a one-quarter symmetric model was used in this research. The 3D computational domain and boundary conditions of the hole with Gaussian shaped wall profile are illustrated in Fig. 6(a). The dimension of the computational domain is 4 mm × 4 mm × 4 mm and the textured area is 2 mm × 2 mm. All the sidewalls are set as a symmetry boundary condition. A rigid no-slip wall boundary condition with 65° static contact angle is imposed at the structured surface. The initial state of water droplet is shown in Fig. 6(b). All the contact angle measurement is a quasi-static state, which means the water droplet has a lower impacting velocity with substrate at initial moment. Thus, in this research, the water droplet has a small distance of 40 µm to the substrate, thus the impacting velocity is about 0.03 m/s and the Weber number is about 0.026. In addition, the total computational time for all the case is 200 ms in order to make sure water droplet has sufficient time to spreading and realize a stable contact angle.

6. Results and discussion

6.1. Printed features evaluation

Fig. 7 shows the WCA measurements on the printed surface and the SEM image of the micro-holes arrays in different pitches with different magnifications. All the components with micro structured surfaces were printed. Better results were obtained with pitch P110 and P150. On the contrary, the geometry of smaller features with pitch of 70 µm (P70) and of 50 µm (P50) was not manufactured accurately and their circular shape was not properly printed. Fig. 8 presents the diameter measurements in five selected areas as mentioned in the geometrical measurements section for P150 and P110. For each area, there were around 20 measurements and the standard deviation was calculated from the same zone. It can be seen that the micro holes are almost evenly separated in different areas. However, in the center of the features in the 5th area more uniform results were obtained with less deviation. 3D surface morphologies of the printed parts in different pitches are represented in Fig. 9. In the smaller features P70 and P50, the depth of the holes were not uniformly printed in all samples, and height variations were observed all over the sample. This dissimilarity could be due to

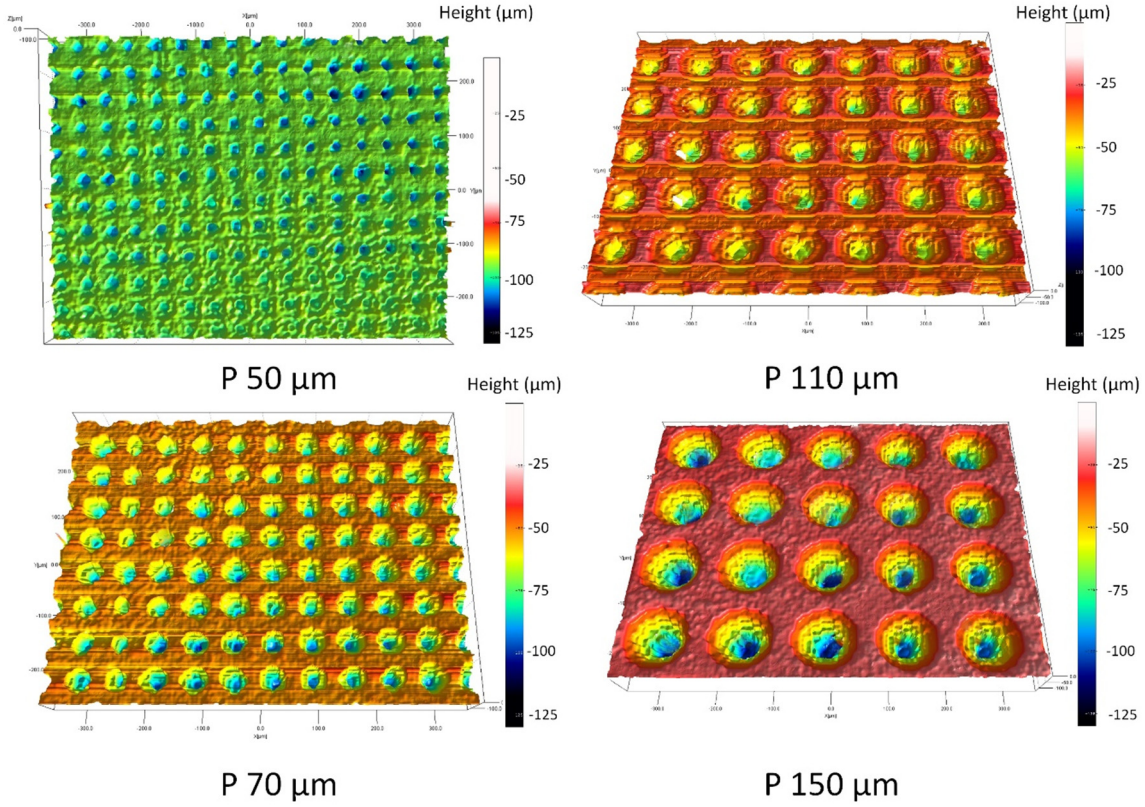

Fig. 9. Surface morphologies with different pitches.

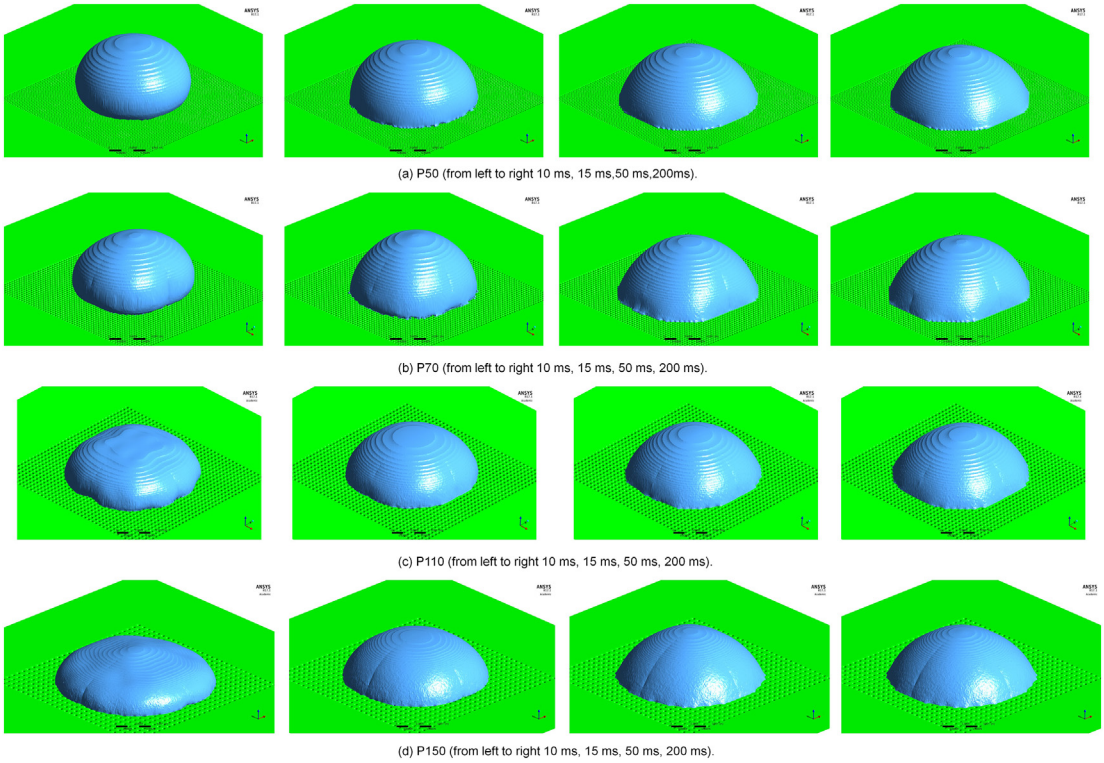

Fig. 10. Variation of 3D shape and dimensions of water droplet.

the shrinkage of the polymer material after post curing or printing process such as pixel spacing limitation in the lower layers near to the bottom of the holes as illustrated in Fig. 7(b) in the highest magnification the transformation of geometry in different layers is visible. Another cause for the depth variation could be due to challenges in the post-processing in cleaning the micro holes to remove the uncured resin. Then, if the uncured resin is not properly removed from the printed holes, in the next step of post-processing in the UV oven it will be cured and affect the geometry of the components with micro holes.

6.2. Simulation values in comparison to experiments

Spreading and recoiling process of water droplets at different substrates are shown in Fig. 10 from 10 to 200 ms. In 10 ms, with increase of pitch, the P110 and P150 substrates have significantly larger spreading diameter than the P50 and P70 substrates. In general, when the water droplet makes an impact on a solid surface, it starts spreading rapidly in the radial direction on the surface. The height of water droplet decreased continuously until the vertical velocity component reduced to zero, which is called impact stage. Then, the droplet started to recoil due to the surface tension effect of the water droplet, which resulted in the raising of the droplet. With further increase in time, the velocity vector decreased gradually, then the water droplet starts to spread on the substrate. At 200 ms, the water droplet reached an equilibrium state. Specially, the P110 and P150 substrates have significantly larger spreading diameter than the P50 and P70 substrates at 10 ms, due to pinning effect induced by micro hole with Gaussian shaped wall profile is more significant for the sample with small pitch.

Fig. 11(a) shows the variation of the maximum height of water droplet on different samples with time. For all the cases at 0–100 ms, the

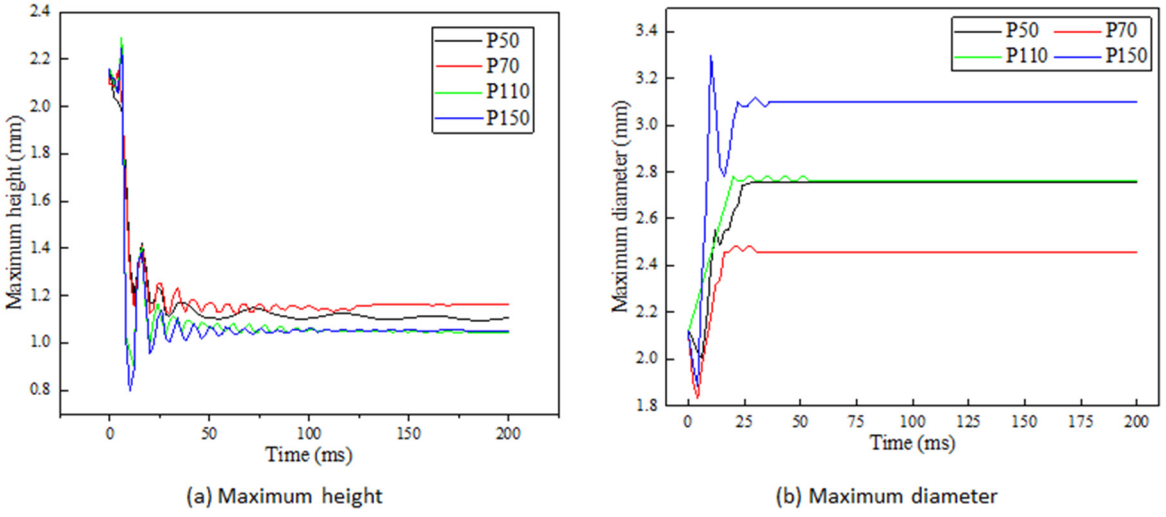

Fig. 11. Variation of maximum height and diameter of water droplet with time.

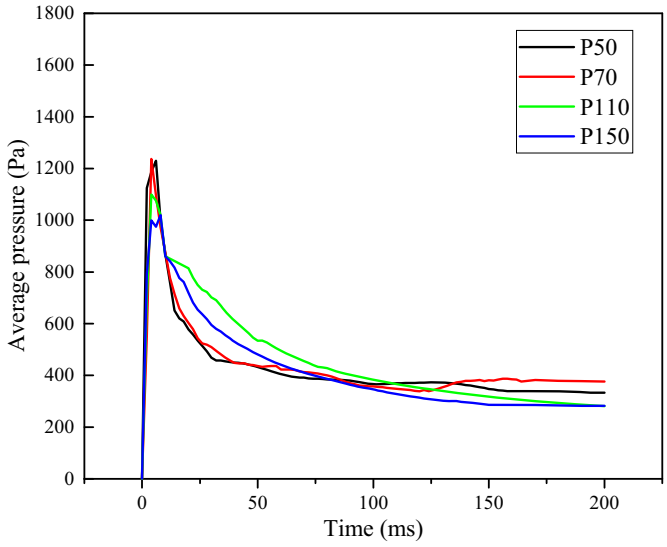

Fig. 12. Variation of average pressure in the substrate.

oscillation of droplet exhibited a form of damping vibration and a decreasing trend of oscillation amplitude was observed. The sample P70 has larger height than others. Fig. 11(b) displays the variation of the maximum diameter of water droplet on different samples with time. First, all the samples have stable maximum diameter after 50 ms, which means the water stop spreading in the horizontal direction. Thus, the vibration only occurs in vertical direction due to the maximum height still change as shown in Fig. 11(a). Especially, the sample P70 has smallest value of stable maximum diameter than other samples, which means the water droplet has less spreading and larger contact angle on the P70 sample than other samples (Fig. 11(b)).

Knowledge of average pressure of air pockets underneath the water droplet during their interaction help reveals the root mechanism behind different wetting state of varied samples. Fig. 12 shows the variation of average pressure in the square area with length of four times of pitch on the substrate. For all substrates, the average air pocket pressure shows an increasing trend in the initial formation stage due to air trapped in the structures gradually. However, the air pockets are metastable, the average pressure of air pockets keep constant in a very short time than start decrease with the wetting process of water droplet. For P70 sample, it has larger pressure than other samples, which help prevent the spreading and wetting of water droplet on the substrate.

In order to evaluate the hydrophobic property of four different surfaces, the apparent contact angle of water droplet at 200 ms was measured based on image processing carried out with a dedicated analysis software (Digimizer). Fig. 13 shows the equilibrium states of water droplets. Fig. 14(a) shows the comparison between the predicted and the measured contact angles. With the increase of the pitch, the contact angle first increased then decreased in both simulation and experimental results with a similar trend. For simulation results, P70 substrate has the maximum value of contact angle with 109.3°. However, the P110 substrate has the maximum contact angle with 113° ±5.4. In order to explain the variation between the experimental and the simulation results the cross sections of the height profile for both the design and additively manufactured components at P110 and P150 are shown in Fig. 14(b). For both P150 and P110 substrates, the actual value of the width of Gaussian hole 6c is larger than optimized value, which result in decrease fraction of solid-liquid contact area. Consequently, the real contact angle will be larger than the predicted value. It concludes that the dissimilar profiles of the additively manufactured sample will affect the pressure of air pockets underneath the water droplet and result in different contact angles in comparison with the design.

7. Conclusion

This research addressed an investigation on direct fabrication of microstructure features by vat photopolymerisation and dynamic behavior simulation for contact angle prediction. Holes with Gaussian shaped wall profile in different pitches were. It was found that this method has enabled the possibility of direct fabrication of the components with micro/nano-structured surfaces by applying proper process parameters and post-processing method. The reliability of the printing procedure was evaluated for uniform microstructured all over the surfaces at P150 and P110. A wettability test was carried out revealing hydrophobic surface for all the samples. Besides, three-dimensional VOF simulations were applied to predict

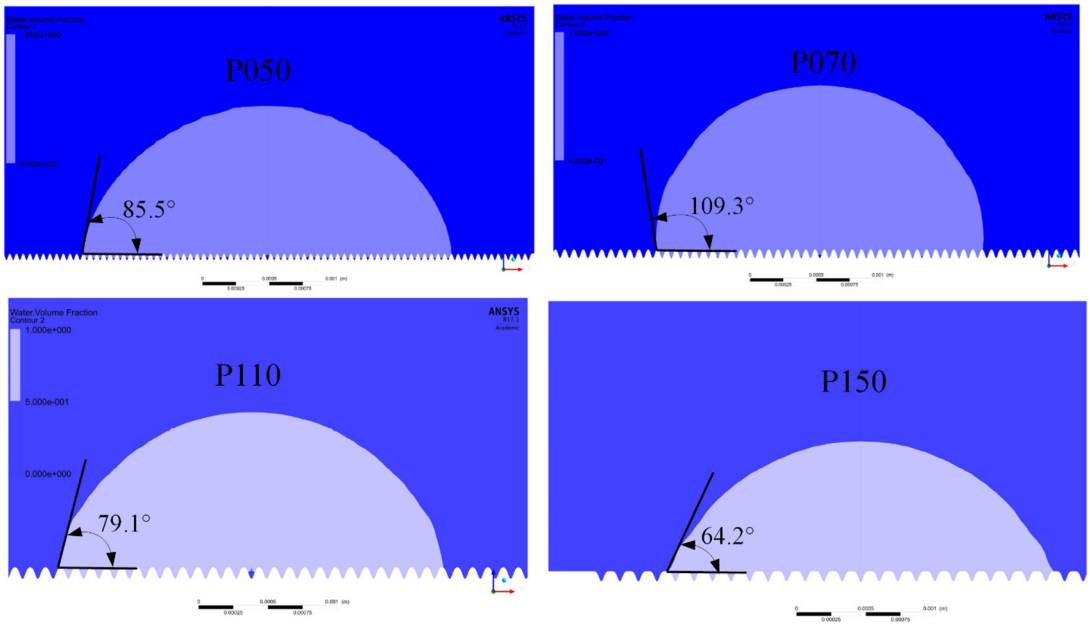

Fig. 13. Apparent contact angle measurement of water droplet at 200 ms.

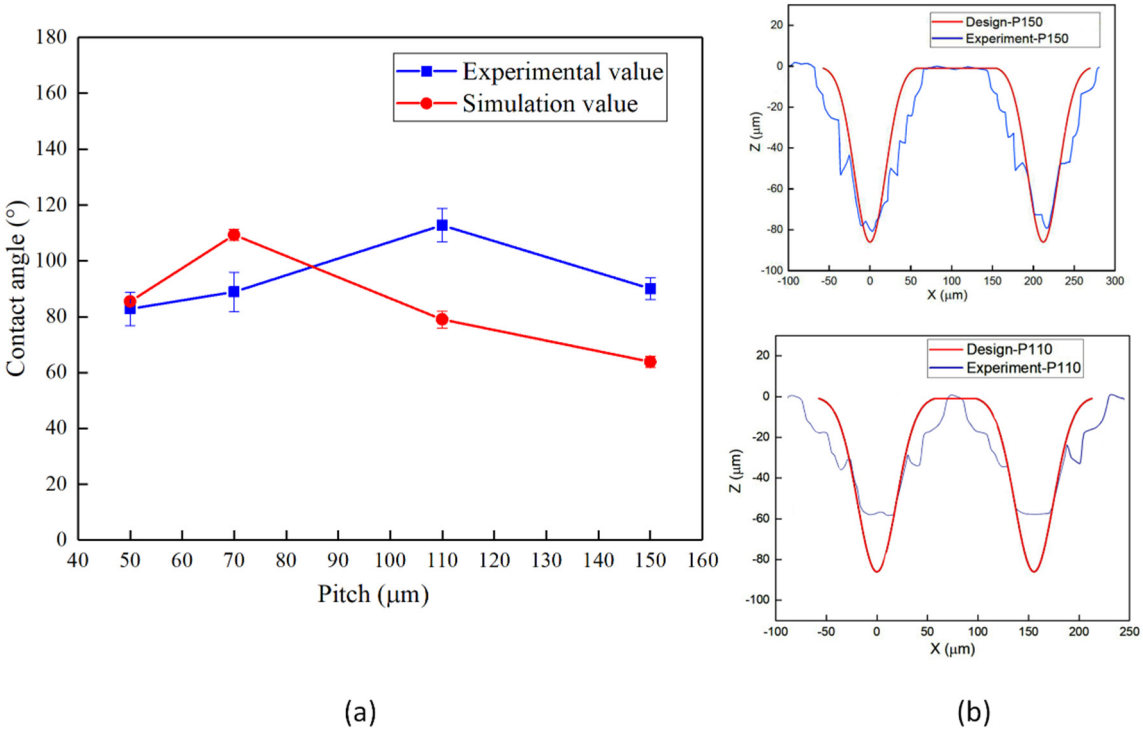

Fig. 14. (a) Comparison between the predicted and measured contact angles (b) comparison between the cross-section of the height profile, design P150 and P110 with experimentally printed components with micro holes.

water droplet angles on the structured surfaces. Both simulation and experiments proved that proper microstructures help improve hydrophilic surface (65°) to hydrophobic surface (with a contact angle of 113° in this research). For P70 sample, it has larger air pocket pressure than other samples, which help prevent the spreading and wetting of water droplet on the substrate and help to form larger contact angle. The average value with the experiments was achieved by the model. The applied model represents a promising method to analyze the structures design prior to manufacturing of the parts and to have a better understanding of the behavior of the contact angle on the features.

CRediT authorship contribution statement

Ali Davoudinejad: Conceptualization, Methodology, Formal analysis, Validation, Data curation, Investigation, Writing - original draft, Visualization, Project administration, Funding acquisition. **Yukui Cai:** Software, Validation, Formal analysis, Data curation, Writing - review & editing, Visualization. **David Bue Pedersen:** Supervision, Resources, Writing - review & editing. **Xichun Luo:** Supervision, Resources, Writing - review & editing. **Guido Tosello:** Supervision, Writing - review & editing, Funding acquisition.

Acknowledgment

The research leading to these results has received funding from the People Programme (Marie Curie Actions) of the European Union's Seventh Framework Programme (FP7/2007-2013) under REA grant agreement no. 609405 (COFUNDPostdocDTU). This research work was undertaken in the context of MICROMAN project ("Process Fingerprint for Zero-defect Net-shape MICROMANufacturing", http://www.microman.mek.dtu.dk/). MICROMAN is a European Training Network supported by Horizon 2020, the EU Framework Programme for Research and Innovation (Project ID: 674801). The authors also acknowledge the use of the EPSRC (EP/K000586/1) funded ARCHIE-WeSt High-Performance Computer at the University of Strathclyde.

References

[1] N. Wang, L. Tang, W. Tong, D. Xiong, Fabrication of robust and scalable superhydrophobic surfaces and investigation of their anti-icing properties, Mater. Des. 156 (2018) 320–328 Oct.
[2] L.B. Boinovich, A.M. Emelyanenko, A.D. Modestov, A.G. Domantovsky, K.A. Emelyanenko, Synergistic effect of superhydrophobicity and oxidized layers on corrosion resistance of aluminum alloy surface textured by nanosecond laser treatment, ACS Appl. Mater. Interfaces 7 (34) (2015) 19500–19508.
[3] K. Jayaramulu, et al., Biomimetic superhydrophobic/superoleophilic highly fluorinated graphene oxide and ZIF-8 composites for oil–water separation, Angew. Chemie Int. Ed. 55 (3) (2016) 1178–1182.
[4] F. Rajab, P.S. Benson, L. Li, K.A. Whitehead, Picosecond laser surface micro/nano texturing of stainless steel as a method to reduce the adhesion of bacteria, Proceedings of LPM2017-the 18th International Symposium on Laser Precision Microfabrication, 2017.
[5] A.C. Lima, J.F. Mano, Micro/nano-structured superhydrophobic surfaces in the biomedical field: part II: applications overview, Nanomedicine 10 (2) (2015) 271–297.
[6] H. Chen, et al., Continuous directional water transport on the peristome surface of Nepenthes alata, Nature 532 (2016) 85–89.
[7] J. Long, et al., Hierarchical micro- and nanostructures induced by nanosecond laser on copper for superhydrophobicity, ultralow water adhesion and frost resistance, Mater. Des. 155 (2018) 185–193 Oct.
[8] H. Ko, H. Yi, H.E. Jeong, Wall and ceiling climbing quadruped robot with superior water repellency manufactured using 3D printing (UNIclimb), Int. J. Precis. Eng. Manuf. Technol 4 (3) (2017) 273–280 Jul.
[9] L.R. Palmer, E. Diller, R.D. Quinn, Toward gravity-independent climbing using a biologically inspired distributed inward gripping strategy, IEEE/ASME Trans. Mechatronics 20 (2) (2015) 631–640.
[10] D. Banoriya, R. Purohit, R.K. Dwivedi, Modern trends in rapid prototyping for biomedical applications, Mater. Today Proc 2 (4–5) (2015) 3409–3418 Jan.
[11] G. Varghese, et al., Fabrication and characterisation of ceramics via low-cost DLP 3D printing, Boletín la Soc. Española Cerámica y Vidr 57 (1) (2018) 9–18 Jan.
[12] S.J. Abbott, P.H. Gaskell, Mass Production of Bio-inspired Structured Surfaces, 2007.
[13] M.T. Northen, C. Greiner, E. Arzt, K.L. Turner, A gecko-inspired reversible adhesive, Adv. Mater. 20 (20) (2008) 3905–3909 Oct.
[14] S.H. Ahn, L.J. Guo, Large-area roll-to-roll and roll-to-plate nanoimprint lithography: a step toward high-throughput application of continuous nanoimprinting, ACS Nano 3 (8) (2009) 2304–2310.
[15] M. Worgull, et al., Sub-μm structured lotus surfaces manufacturing, Microsyst. Technol. 15 (8) (2009) 1327–1333.
[16] A. Milionis, et al., Water-repellent approaches for 3-D printed internal passages, Mater. Manuf. Process. 31 (9) (2016) 1162–1170 Jul.
[17] M. Röhrig, M. Thiel, M. Worgull, H. Hölscher, 3D direct laser writing of nano- and microstructured hierarchical gecko-mimicking surfaces, Small 8 (19) (2012) 3009–3015 Oct.

[18] A.P. Zhang, et al., Rapid fabrication of complex 3D extracellular microenvironments by dynamic optical projection stereolithography, Adv. Mater. 31 (31) (2012) 4266–4270.
[19] W. Zhu, X. Ma, M. Gou, D. Mei, K. Zhang, S. Chen, 3D printing of functional biomaterials for tissue engineering, Curr. Opin. Biotechnol. 40 (2016) 103–112 Aug.
[20] S.M. Ahmadi, R. Hedayati, R.K. Ashok Kumar Jain, Y. Li, S. Leeflang, A.A. Zadpoor, Effects of laser processing parameters on the mechanical properties, topology, and microstructure of additively manufactured porous metallic biomaterials: a vector-based approach, Mater. Des. 134 (2017) 234–243 Nov.
[21] H. Fayazfar, et al., A critical review of powder-based additive manufacturing of ferrous alloys: process parameters, microstructure and mechanical properties, Mater. Des. 144 (2018) 98–128 Apr.
[22] J.A. Harris, R.E. Winter, G.J. McShane, Impact response of additively manufactured metallic hybrid lattice materials, Int. J. Impact Eng. 104 (2017) 177–191.
[23] R. Lu, S. Chandrasekaran, W.L. Du Frane, R.L. Landingham, M.A. Worsley, J.D. Kuntz, Complex shaped boron carbides from negative additive manufacturing, Mater. Des. 148 (2018) 8–16 Jun.
[24] Y. Cai, et al., Superhydrophobic structures on 316L stainless steel surfaces machined by nanosecond pulsed laser, Precis. Eng. 52 (October 2017) (2018) 266–275.
[25] A. Davoudinejad, G. Tosello, M. Annoni, Influence of the worn tool affected by built-up edge (BUE) on micro end-milling process performance: a 3D finite element modeling investigation, Int. J. Precis. Eng. Manuf. 18 (10) (2017) 1321–1332.
[26] D.S.J. Al-Saedi, S.H. Masood, M. Faizan-Ur-Rab, A. Alomarah, P. Ponnusamy, Mechanical properties and energy absorption capability of functionally graded F2BCC lattice fabricated by SLM, Mater. Des. 144 (2018) 32–44.
[27] C. Ling, A. Cernicchi, M.D. Gilchrist, P. Cardiff, Mechanical behaviour of additively-manufactured polymeric octet-truss lattice structures under quasi-static and dynamic compressive loading, Mater. Des. 162 (2019) 106–118 Jan.
[28] S. Gangireddy, B. Gwalani, K. Liu, E.J. Faierson, R.S. Mishra, Microstructure and mechanical behavior of an additive manufactured (AM) WE43-Mg alloy, Addit. Manuf 26 (2019) 53–64 Mar.
[29] A. Beharic, R. Rodriguez Egui, L. Yang, Drop-weight impact characteristics of additively manufactured sandwich structures with different cellular designs, Mater. Des. 145 (2018) 122–134.
[30] Y.H. Yeong, J. Burton, E. Loth, I.S. Bayer, Drop impact and rebound dynamics on an inclined superhydrophobic surface, Langmuir 30 (40) (2014) 12027–12038.
[31] C.M. González-Henríquez, M.A. Sarabia-Vallejos, J. Rodriguez-Hernandez, Polymers for additive manufacturing and 4D-printing: materials, methodologies, and biomedical applications, Prog. Polym. Sci. xxx (Mar. 2019) xx–xxx.
[32] S. Bakhshian, S.A. Hosseini, N. Shokri, Pore-scale characteristics of multiphase flow in heterogeneous porous media using the lattice Boltzmann method, Sci. Rep. 9 (1) (2019) 3377.
[33] M. Shams, A.Q. Raeini, M.J. Blunt, B. Bijeljic, A numerical model of two-phase flow at the micro-scale using the volume-of-fluid method, J. Comput. Phys. 357 (2018) 159–182.
[34] W.Z. Yuan, L.Z. Zhang, Lattice Boltzmann simulation of droplets impacting on superhydrophobic surfaces with randomly distributed rough structures, Langmuir 33 (3) (2017) 820–829.
[35] S. Khan and J. K. Singh, "Wetting transition of nanodroplets of water on textured surfaces: a molecular dynamics study," Mol. Simul., vol. 40, no. 6. Taylor & Francis, pp. 458–468, 2014.
[36] W. Xu, Z. Lan, B.L. Peng, R.F. Wen, X.H. Ma, Effect of surface free energies on the heterogeneous nucleation of water droplet: a molecular dynamics simulation approach, J. Chem. Phys. 142 (5) (2015), 054701.
[37] K. Connington, T. Lee, Lattice Boltzmann simulations of forced wetting transitions of drops on superhydrophobic surfaces, J. Comput. Phys. 250 (2013) 601–615.
[38] L.Z. Zhang, W.Z. Yuan, A lattice Boltzmann simulation of coalescence-induced droplet jumping on superhydrophobic surfaces with randomly distributed structures, Appl. Surf. Sci. 436 (2018) 172–182.
[39] C. Antonini, A. Amirfazli, M. Marengo, Drop impact and wettability: from hydrophilic to superhydrophobic surfaces, Phys. Fluids 24 (10) (2012).
[40] C.W. Hirt, B.D. Nichols, Volume of fluid (VOF) method for the dynamics of free boundaries, J. Comput. Phys. 39 (1) (1981) 201–225.
[41] I. Malgarinos, N. Nikolopoulos, M. Marengo, C. Antonini, M. Gavaises, VOF simulations of the contact angle dynamics during the drop spreading: standard models and a new wetting force model, Adv. Colloid Interf. Sci. 212 (2014) 1–20.
[42] P.R. Gunjal, V.V. Ranade, R.V. Chaudhari, Dynamics of drop impact on solid surface: experiments and VOF simulations, AICHE J. 51 (1) (2005) 59–78.
[43] J. Xu, Y. Chen, J. Xie, Non-dimensional numerical study of droplet impacting on heterogeneous hydrophilicity/hydrophobicity surface, Int. J. Heat Mass Transf. 116 (2018) 951–968.
[44] K. Murugadoss, P. Dhar, S.K. Das, Role and significance of wetting pressures during droplet impact on structured superhydrophobic surfaces, Eur. Phys. J. E 40 (1) (2017) 1–10.
[45] A.S.T.M. International, F2792-12a - standard terminology for additive manufacturing technologies, Rapid Manuf. Assoc. (2013) 10–12.
[46] E. Tyge, J. J. Pallisgaard, M. Lillethorup, N. G. Hjaltalin, M. K. Thompson, and L. H. Clemmensen, "Characterizing digital light processing (DLP) 3D printed primitives," in Image Analysis: 19th Scandinavian Conference, SCIA 2015, Copenhagen, Denmark, June 15–17, 2015. Proceedings, R. R. Paulsen and K. S. Pedersen, Eds. Cham: Springer International Publishing, 2015, pp. 302–313.
[47] R. Liska, et al., Photopolymers for rapid prototyping, J. Coatings Technol. Res 4 (4) (2007) 505–510.
[48] A.R. Jørgensen, Design and development of an improved direct light processing (DLP) platform for precision additive manufacturing, Technical University of Denmark (DTU), 2015.
[49] A. Davoudinejad, M.M. Ribo, D.B. Pedersen, A. Islam, G. Tosello, Direct fabrication of bio-inspired gecko-like geometries with vat polymerization additive manufacturing method, J. Micromechanics Microengineering 28 (8) (2018).
[50] Visitech, [Online]. Available: https://visitech.no/products/luxbeam-rapid-system.
[51] O.J. Guy, K.-A.D. Walker, Graphene functionalization for biosensor applications, Silicon Carbide Biotechnol (Jan. 2016) 85–141.
[52] T. Young, An essay on the cohesion of fluids author(s): Thomas Young source: Philosophical Transactions of the Royal Society of London, Vol. 95 (1805), pp. 65-87 published by, Philos. Trans. R. Soc. London 95 (1805) (1805) 65–87.
[53] "16.3.1 Overview and Limitations of the VOF Model."
[54] G. K. Batchelor, "An Introduction to Fluid Dynamics," Book. p. 631, 1967.
[55] J.U. Brackbill, D.B. Kothe, C. Zemach, A continuum method for modeling surface tension, J. Comput. Phys. 100 (2) (1992) 335–354.